Journal of
Materials Chemistry A

Materials for energy and sustainability

Accepted Manuscript

This article can be cited before page numbers have been issued, to do this please use: A. M. Arcidiacono, C. Ruchlin, G. M. McLeod, D. Pattadar, S. Lindbom, A. J. Robb, S. Ayad, N. R. Dos Santos, I. Alabugin, S. S. Saavedra and K. Hanson, *J. Mater. Chem. A*, 2024, DOI: 10.1039/D4TA05156D.

ROYAL SOCIETY OF CHEMISTRY

rsc.li/materials-a

View Article Online
DOI: 10.1039/D4TA05156D

ARTICLE

Structural Insights to Metal Ion Linked Multilayers on Metal Oxide Surfaces via Energy Transfer and Polarized ATR Measurements

Received 00th January 20xx,
Accepted 00th January 20xx

DOI: 10.1039/x0xx00000x

Ashley Arcidiacono,[a] Cory Ruchlin,[b] Grace M. McLeod,[a] Dhruba Pattadar,[c] Sarah Lindbom,[a] Alex J. Robb,[a] Suliman Ayad,[a] Nikolas R. Dos Santos,[a] Igor V. Alabugin,[a] S. Scott Saavedra,[c] Kenneth Hanson[a]

Metal ion linked multilayers offer a means of controlling interfacial energy and electron transfer for a range of applications including solar energy conversion, catalysis, sensing, and more. Despite the importance of structure to these interlayer transfer processes, little is known about the distance and orientation between the molecules/surface of these multilayer films. Here we gain structural insights into these assemblies using a combination of UV-Vis polarized visible attenuated total reflectance (p-ATR) and Förster Resonance Energy Transfer (FRET) measurements. The bilayer of interest is composed of a metal oxide surface, phosphonated anthracene molecule, Zn(II) linking ion, and a platinum porphyrin with one (P1), two (P2), or three (P3) phenyl spacers between the chromophoric core and the metal ion binding carboxylate group. As observed by both time-resolved emission and transient absorption, the FRET rate and efficiency decreases with an increasing number of phenyl spacers (P1 > P2 > P3). However, from p-ATR measurements there is a change in orientation of porphyrins in the bilayer which prohibits the determination of the orientation factor (κ^2) across the series. Instead, we narrow the scope of viable structures by determining the best agreement between experimental and calculated FRET efficiencies. Additionally, we provide evidence that suggests, for the first time, that the bilayer structure is similar on both planar and mesoporous substrates.

Introduction

The assembly of multiple molecular components at a metal oxide surface is of interest for their application in solar energy conversion, photocatalysis, sensing and more.[1–3] Of the strategies for combining molecules at an interface (e.g., electrostatics, co-deposition, covalent dyads, etc.),[4] metal ion linked multilayers are appealing because 1) they are generated via a simple step-wise soaking procedure, 2) they avoid the synthetic complexities of covalently-bound dyads, 3) the components are modular, and 4) they circumvent the surface area limitation of co-deposited films.[3] The strategic selection of components (e.g., chromophores, catalysts, electron donor/acceptor, etc.) and their proximity to the surface can be used to facilitate directional energy and electron transfer as desired for their application in photon upconversion,[5–7] solar energy conversion,[8] photocatalysis,[9–11] molecular rectifying interfaces,[12–15] and electrochromism.[16]

The rate and efficiency of these interfacial energy and electron transfer events are not only dependent on the energetics of the components but also the structure of the assembly (i.e., the distance and orientation between the molecules/surface). In terms of structural insights into metal ion linked multilayers, the molecular and metal ion ratios have been quantified using UV-Vis spectroscopy, XPS, and mass spectrometry.[3,17,18] Metal ion coordination and multilayer thickness has been determined from IR spectroscopy, atomic force microscopy, ellipsometry, X-ray photoelectron spectroscopy, and UV-Vis spectroscopy.[3,19–22]

Recently, our team was the first to use polarized UV-Vis attenuated total reflectance (p-ATR) spectroscopy to determine the transition dipole moment orientation of molecular monolayers[23] as well as in metal ion linked bilayer[24] and trilayer films.[25] While p-ATR, and other grazing angle techniques (e.g., XRR, IRRAS, etc.),[26–28] lend some insight into the structure at molecule-metal oxide interfaces, they suffer from two fundamental limitations relevant to the materials discussed here. First, is that these measurements are performed on planar surfaces which may or may not accurately represent the structure on mesoporous substrates.[29] Second, they can only provide information about the molecular orientation relative to the substrate.[30,31] The later issue is particularly problematic for

[a] Department of Chemistry and Biochemistry, Florida State University, Tallahassee, Florida 32306, United States.
[b] Department of Chemistry, McGill University, 801 Sherbrooke Street West, Montreal, Quebec, Canada H3A 0B8.
[c] Department of Chemistry and Biochemistry, University of Arizona, Tucson, Arizona 85721, United States .
Electronic Supplementary Information (ESI) available: [details of any supplementary information available should be included here]. See DOI: 10.1039/x0xx00000x

View Article Online
DOI: 10.1039/D4TA05156D

multimolecular systems because, in the absence of an additional frame of reference (i.e., the azimuthal angle), they cannot provide the orientation of the molecules relative to each other.[25]

In this manuscript we describe our effort to address these shortcomings by using p-ATR in conjunction with Förster Resonance Energy Transfer (FRET) measurements to determine the structure of a metal ion-linked bilayer assembly. The bilayer of interest is shown in Figure 1 and is composed of a mesoporous zirconium oxide substrate (ZrO_2), phosphonated anthracene molecule (**A**), Zn(II) linking ion, and a carboxylated, unsymmetric porphyrin (**PX**, were X = the number of phenyl spacers, 1, 2, or 3).

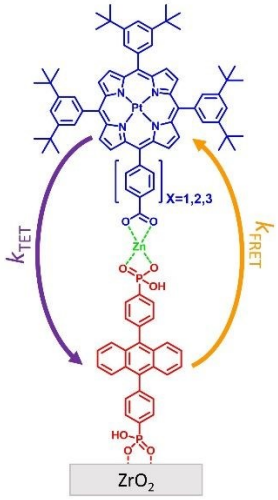

Fig. 1 General depiction of a metal ion linked bilayer composed of a ZrO_2 substrate, **A** (red), Zn(II) linking ion (green), and **PX** (blue) where X is the number of phenyl spacers. The directionality and rate constant for TET and FRET are depicted in purple and orange, respectively.

This bilayer (ZrO_2-**A**-Zn-**PX**) was chosen because it is a derivative of our previously studied molecular photon upconversion films,[5,24,32,33] and it has appropriate energetics for ^{3}**PX*** to **A** triplet energy transfer (TET) and ^{1}**A*** to **PX** FRET.[32] The latter energy transfer process, FRET, is particularly important here as it has well-known distance and orientation dependences as described in equations 1-2.[34–36]

$$E = \frac{1}{1+\left(\frac{r_{DA}}{R_0}\right)^6} \quad (1)$$

$$R_0 = 9780(\kappa^2 \Phi_D n^{-4} J)^{1/6} \quad (2)$$

where E is the FRET efficiency, r_{DA} is the separation between donor and acceptor, R_0 is the Förster radius, J is the spectral overlap integral, n is the refractive index, Φ_D is the fluorescence quantum yield of the donor, and κ^2 is the orientation factor.

$$\kappa^2 = (\cos\alpha - 3\cos\beta\cos\gamma)^2 \quad (3)$$

The orientation factor, κ^2, is dependent on the angle between donor dipole moment and radial vector (α), acceptor dipole moment and radial vector (β), and donor and acceptor dipole moments (γ).

For a fixed pair of chromophores where J, n, and Φ_D are constant, then the relationship between measured values of E with respect to systematic variation in r_{DA} (i.e., n=1-3 in Figure 1) could be used to determine κ^2 and the relative orientation of the molecules in the bilayer film.[37,38] That, in conjunction with p-ATR measurements (i.e., the orientation relative to the surface), could provide a unique average geometry of the bilayer film.

Below, we recount our effort using time-resolved emission and transient absorption to quantify the energy transfer rates and yields in the bilayer film depicted in Figure 1. p-ATR is then used to determine the orientation of the chromophores relative to the surface. Due to an orientation change between **P1**, **P2**, and **P3** and the added complexity of the transition plane of **PX**, we were unable to determine a unique structure. Instead, we used calculated and experimental FRET efficiencies to narrow the scope of possible structures.

Experimental

Materials

Zinc acetate, boron trifluoride diethyl etherate, chloroform, benzonitrile, potassium hydroxide, methanol, dichloromethane, hexanes, and acetonitrile were purchased from Sigma Aldrich and used without any further purification. 3,5-Di-tert-butylbenzaldehyde was purchased from Sigma Aldrich and recrystallized from ethanol three times prior to use. 2,3-dichloro-5,6-dicyano-p-benzoquinone (DDQ) and Methyl 4-formyl benzoate were purchased from Alfa Aesar and used without further purification. Pyrrole was purchased from Sigma-Aldrich and distilled over calcium hydride (Sigma Aldrich) prior to use. Benzonitrile was purchased from Sigma Aldrich and distilled prior to use. Melatonix film and Vac'n Fill syringes were purchased from Solaronix. Glass substrates were acquired from Hartford Glass Co. Micro glass cover slides (18 × 18 mm) were obtained from VWR. ZrO_2 solgel pastes were prepared following previously reported procedures.[39] **A**[40] and **P3**[41] were synthesized following previously reported procedure. Synthetic details for **P1** and **P2** can be found in SI.

Film Loading

Mesoporous ZrO_2 on glass substrates was functionalized with monolayers of **A** via soaking in a loading solution of 200 μM **A** in DMSO for 48 h. For the coordination of Zn(II), films were then submerged in a solution of $Zn(CH_3COO)_2$ in MeOH (500 μM) for 2 h, followed by 150 μM **P1**/**P2** or 9.0 mg in 60 mL of **P3** in 1:1 chloroform:methanol until an **A**:**PX** ratio of ~10:1 was reached (15 minutes for **P1**/**P2** and 3 hrs for **P3**), resulting in ZrO_2-A-Zn-**PX**. Surface coverage isotherms can be found in SI. Films on planar ITO were loaded via a liquid flow cell using the conditions listed in Table S5. The adsorption isotherms (obtained with transverse magnetic polarized light) can be found in SI.

Absorption Spectroscopy

Absorption spectra were acquired using an Agilent 8453 UV-visible photo diode array spectrophotometer. Thin film absorption spectra were collected via placing functionalized metal oxide films perpendicular to the detection path.

Steady-state and Time-Resolved Emission

An Edinburgh FLS980 fluorescence spectrometer was used to obtain emission spectra. A 450 W Xe lamp coupled with a single grating (1800 l/mm, 250 nm blaze) Czerny–Turner monochromator was used as output to excite the samples. Sample emission was passed through a 435 nm long pass filter then a single grating (1800 l/mm, 500 nm blaze) Czerny–Turner monochromator and then detected by a Peltier-cooled Hamamatsu R928 photomultiplier tube. Time-resolved emission was collected at room temperature using the same Edinburgh FLS980 fluorescence spectrometer. Emission decay kinetics were obtained using multichannel scaling (MCS; >1 μs) or time-correlated single photon counting (TCSPC; <1 μs) with data collection until 10,000 counts. MCS measurements utilized excitation output from a 60 W microsecond flashlamp (pulse width <2.5 μs) at a 100 Hz repetition rate passed through a single grating (1800 l/mm, 250nm blaze) Czerny–Turner monochromator. Excitation for TCSPC was generated by an Edinburgh EPL-360 ps pulsed light emitting diode (360 ± 10 nm, pulse width 890 ps) with emission was then passed through a single grating (1800 l/mm, 500 nm blaze) Czerny– Turner monochromator and detected by a Peltier-cooled Hamamatsu R928 photomultiplier tube. For kinetics on films, a biexponential fitting using an IRF deconvolution[24] was used and a weighted average lifetime is reported.

Transient Absorption

Transient absorption measurements were obtained using a HELIOS Fire transient absorption spectrometer (Ultrafast Systems). The spectrometer was coupled to the output of a Vitara-S Coherent Ti:sapphire laser amplifier using a 1 kHz Coherent Revolution-50 pump laser (5 mJ pulse, 150 fs fwhm at 800 nm). This output was split into a pump and probe beam. The probe was passed through a delay stage while the pump traveled through an optical parametric amplifier (OPerA Solo from Coherent) for wavelength selection. A white light supercontinuum, used for the probe, was produced by a sapphire crystal. The pump and probe beam were then overlapped on the sealed, deaerated sample that was mounted in a rastering stage. Difference spectra and single wavelength kinetics were collected averaging 3 times and holding for 3 seconds, with an exponential point acquisition beginning with 0.01 ps steps and totalling to 250 points. Chirp correction was processed using the Surface Xplorer software package from Ultrafast Systems.

Polarized Visible Attenuated Total Reflectance (p-ATR)

ATR spectroscopy measurements were conducted using a spectrometer described previously.[42] ITO-coated glass slides (Thin Film Devices) served as planar waveguides. A Xe lamp (polarized and collimated) was coupled into and out of the waveguide using two BK7 (n = 1.51) prisms. The outcoupled light was directed into a monochromator (Newport MS260i) using a fiber-optic cable and was detected by a CCD camera (Andor iDus420A).The mean tilt angles of the absorbance dipoles of **A** in monolayer films and **A** and porphyrins in bilayer films were determined using previously described methods.[31]

Atomic Layer Deposition (ALD)

Glass microscope cover slides (VWR) were first sonicated in an HCl/Ethanol (15/85% mix) solution for 20 minutes and then ethanol for 20 mins. The glass was then dried under a stream of air. Atomic layer deposition (ALD) was performed using a Fiji G2 plasma enhanced atomic layer deposition system (Veeco). Tetrakis(dimethylamido)zirconium (TDMAZ) was purchased (STREM Chemical) as a precursor for deposition. Recipe for O_2 plasma deposition was obtained from the manufacturer and performed without modification. Briefly, the instrument heaters controlling the reactor, chuck, and delivery lines were set to 250 °C and the precursor was heated to 75 °C. The samples were then placed into the instrument platter, sealed inside the chuck, and the chuck and reactor were then pumped down from ambient pressure to vacuum (1×10^{-6} torr). Once under vacuum, the sample platter was then transferred to the reactor to begin the ALD process. Once in the reactor, the recipe pulsed the precursor at 30 sccm for 0.25 seconds, held for 5 seconds, applied 300 watts of plasma for 6 seconds, held for 5 seconds, and then repeated this process until the predetermined number of cycles was performed (40 cycles, ~1 Å/cycle) to generate a ~4 nm planar ZrO_2 film.

Results and Discussion

Synthesis and Surface Loading

The molecules of interest for this study are shown in Figure 1. Phosphonated anthracene derivative **A** was chosen as the FRET donor because it has a relatively high emission quantum yield ($\Phi_{ZrO_2\text{-}A}$ = 0.53),[40] and its transition dipole moment is known and aligned with the long axis of the molecule (i.e., across the 9,10 carbon atoms of anthracene).[43] Furthermore, its properties at the interface have been extensively investigated in our lab.[32,40,44]

As noted above, and in the molecular photon upconversion literature,[7,45] Pt(II) porphyrin molecules make a well-known TET and FRET pair with anthracene derivatives. In contrast to our previously studied Pt(II) 5,10,15,20-(tetra-4-carboxyphenyl)porphyrin containing bilayers,[32,46] the unsymmetric **P1-3** derivatives were designed to have only one carboxyl group (i.e., a single Zn(II) coordination site) and the distance from **A** is systematically increased via the addition of phenylene spacing groups. **P1-3** were prepared using modification of previously published procedures with details provided in the supporting information.[41,47,48]

View Article Online DOI: 10.1039/D4TA05156D

P1-3 exhibit nearly identical Soret (400 nm) and Q-band (512 nm) features (Figure S1) indicating that the number of phenylene groups had minimal impact on ground state absorption of the porphyrin core. Similarly, the extinction coefficient and peak ratios of **P1-3** were comparable to that of symmetric Pt(II) porphyrins,[32] suggesting that differences in meso-phenyl substitution did not introduce asymmetry to the porphyrins' degenerate transitions.[49]

The bilayer film was assembled on mesoporous ZrO_2. ZrO_2 was chosen due to its relatively high conduction band potential, inhibiting excited state electron transfer from **A** or **PX**.[50] Consequently, the photophysical properties of the assembly can be studied without concern of excited state quenching *via* interfacial electron transfer.[32]

Metal ion-linked multilayers were assembled using a stepwise soaking procedure. ZrO_2 films were first soaked in a 300 µM DMSO solution of **A** for 24 hours and then a 500 µM methanol solution of $Zn(OAc)_2$ for 2 hours. ZrO_2-**A**-Zn films were then soaked in a 150 µM solution of **P1** or **P2** in chloroform:methanol (1:1, v/v) for 2 hours resulting in the ZrO_2-**A**-Zn-**PX** bilayers. The loading isotherms for **P1** and **P2** on ZrO_2-**A**-Zn are provided in the supporting information (Figures S4-5). **P3** exhibited notably lower solubility than that of **P1** and **P2**. Consequently, ZrO_2-**A**-Zn-**P3** bilayer films were prepared by soaking ZrO_2-**A**-Zn in a saturated solution (9 mg in 60 mL) of **P3** in chloroform:methanol (1:1, v/v). A maximum surface loading of **P3** was achieved in 3 hours which, based on the UV-Vis spectra, resulted in an ~10:1 ratio for **A**:**P3**. For all subsequent measurements, the ZrO_2-**A**-Zn-**P1** and ZrO_2-**A**-Zn-**P2** films were prepared at the same 10:1 **A**:**PX** ratio to minimize any possible impact of chromophore ratios on excited state dynamics.

The absorption spectra of ZrO_2-**A**-Zn-**P1** and its components are shown in Figure 2 with spectra for all bilayer films provided in Figure S6. Consistent with previous reports, the bilayer film exhibits the additive features of its components indicating minimal direct coupling between the **A** and **PX** chromophores. Also highlighted are the 360 nm and 512 nm excitation wavelengths for selective excitation of **A** and **PX**, respectively.

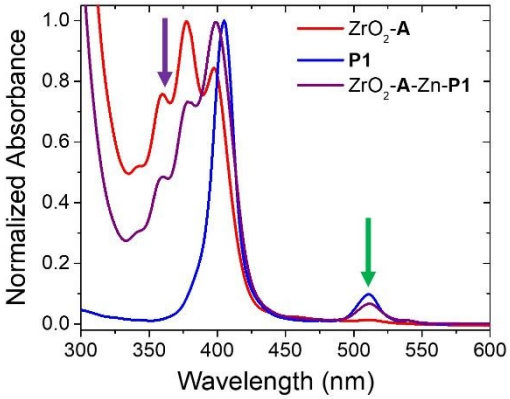

Fig. 2 Absorption spectra of ZrO_2-**A**, ZrO_2-**A**-Zn-**P1**, and **P1** in chloroform:methanol (1:1, v/v). Purple and green arrows indicate 360 and 512 nm excitation wavelengths, respectively.

Excited State Energy Transfer

^{1}**A*** to **PX** energy transfer was first probed using time-resolved emission spectroscopy (TRES) and the results are shown in Figure 3. Under 360 nm excitation, emission features from ZrO_2-**A** are consistent with fluorescent decay from the ^{1}**A*** state,[32] whose kinetics at 460 nm could be fit with a biexponential function. The amplitude (A_x) and lifetime (τ_x) for each component as well as the weighted average lifetime ($\tau_{w(A)}$) are summarized in Table S1. Multiexponential fitting of even a single surface bound emitter is common and is often attributed to inhomogeneous local environments in the film.[32,51] Nonetheless, the weighted average lifetime of 5 ns is reasonably consistent with that observed in solution.[40]

In the ZrO_2-**A**-Zn-**PX** films, following preferential excitation of **A** at 360 nm, **A** emission is quenched with the decay rate increasing in the order of **P3** < **P2** ≈ **P1** (Figure 3). This observation is consistent with excited state quenching of **A** via ^{1}**A*** to **PX** Förster Resonance Energy Transfer (FRET), whose efficiency decreases as the number of phenyl spacers increases (X in Figure 1). The excited state decay for **P1-** and **P2**-containing films were near our instrument response function (IRF ≈ 1 ns) but decay kinetics from the ZrO_2-**A**-Zn-**P3** films were fit using IRF deconvolution, giving a weighted average lifetime of 3.1±0.3 ns.

Assuming that energy transfer to **P3** is the only additional quenching mechanism introduced in the bilayer, then the rate constant for energy transfer (k_{FRET}) can be estimated using equation 4:

$$k_{\mathrm{FRET}} = \frac{1}{\tau_{\mathrm{bl}}} - \frac{1}{\tau_{\mathrm{A}}} \qquad (4)$$

where τ_A and τ_{bl} are the weighted average lifetime for anthracene emission in the ZrO_2-**A**, and ZrO_2-**A**-Zn-**P3** films, respectively.[32] However, the calculated rate constant of 1.0±0.4 × 10^8 s^{-1} is a low end estimate of k_{FRET} because 1) this measurement only captures kinetics after 1 ns and 2) not all **A** molecules are necessarily involved in the energy transfer process resulting in contributions from the intrinsic emission decay of ^{1}**A***.[41]

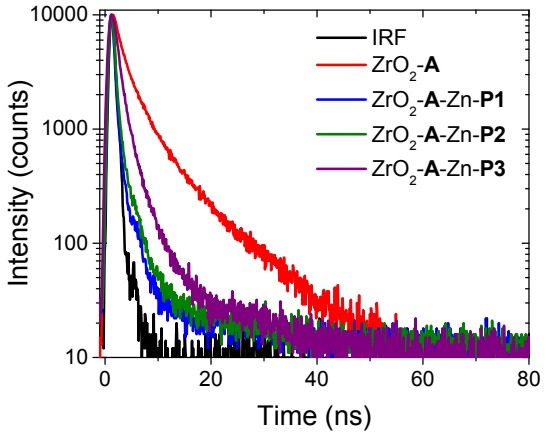

Fig. 3 Time-resolved emission at 460 nm for ZrO_2-**A** and ZrO_2-**A**-Zn-**PX** in MeCN (λ_{ex}=360 nm).

View Article Online
DOI: 10.1039/D4TA05156D

ARTICLE

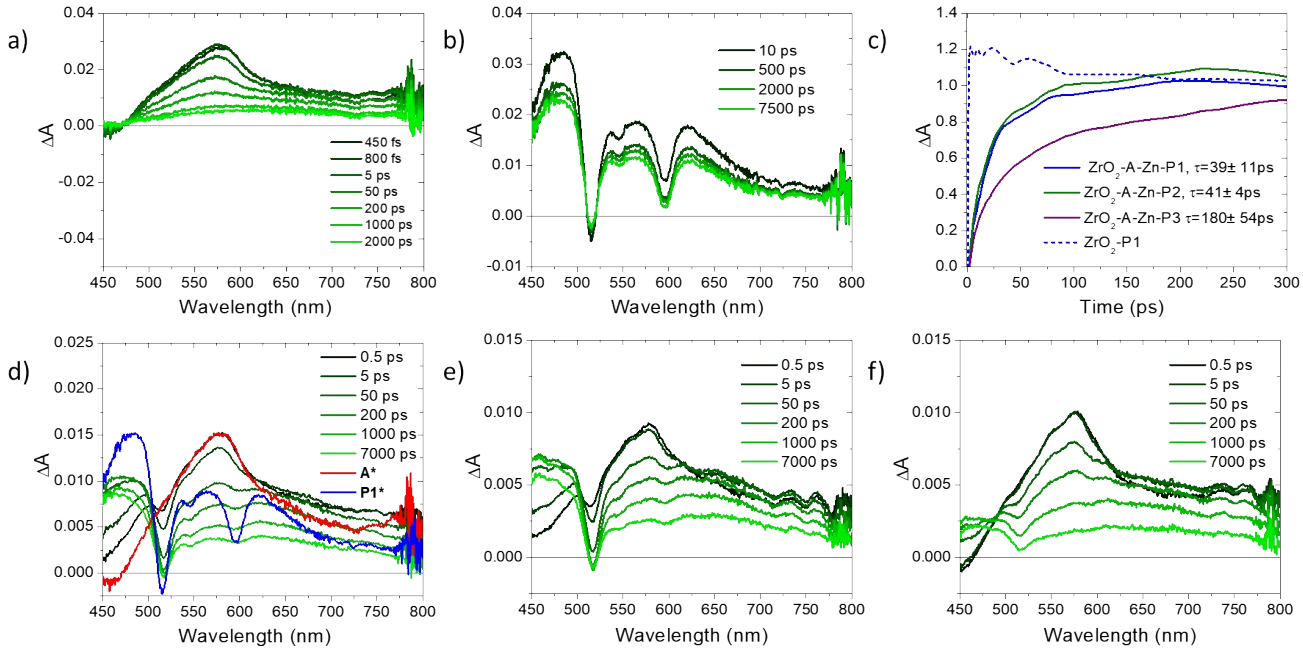

Fig. 4 Transient absorption spectra for a) ZrO_2-**A** (λ_{ex} = 360 nm) and b) ZrO_2-**P1** (λ_{ex} = 512 nm). (c) Single wavelength kinetics for ZrO_2-**A**-Zn-**PX** at 460 nm (λ_{ex} = 360 nm) and ZrO_2-**P1** at 460 nm (λ_{ex} = 512 nm). Transient absorption spectra for ZrO_2-**A**-Zn-**PX** where d) X = 1, e) X = 2, and f) X = 3 (λ_{ex} = 360 nm). Red and blue overlays in (d) are spectra at 500 fs for ZrO_2-**A** and 10 ps ZrO_2-**P1**, respectively. All samples were measured in nitrogen deaerated MeCN.

To circumvent these limitations, we performed ultrafast transient absorption (TA) spectroscopy, and the results are shown in Figure 4 with the kinetic fits summarized in Table S2. For the ZrO_2-**A** film excited at 360 nm, there is a prominent excited state absorption (ESA) feature at 575 nm that decays in ~2 ns, in line with ^{1}**A*** emission described above. Upon excitation with 512 nm, ZrO_2-**P1** exhibits a ground state bleach for the Q-band at ~515 nm and broad excited state absorption from 400-800 nm. These features persist well beyond the instrument time resolution of 7 ns and are in agreement with rapid intersystem crossing followed by excited state decay from the triplet state of **P1** (^{3}**P1***).[41,52,53]

Under 360 nm excitation of **A**, all three bilayer films are initially dominated by the ESA of ^{1}**A*** followed by the appearance of ^{3}**PX*** features. The late time contribution of ^{3}**PX*** is notably lower in the ZrO_2-**A**-Zn-**P3** film, where energy transfer is expected to be slower and less efficient. The kinetics for the growth of **PX** excited states were monitored at 460 nm (i.e., the isosbestic point for ZrO_2-**A**) and the results are shown in Figure 4c. For all three films, there is a growth of ^{3}**PX*** ESA that largely plateaus by 400 ps and persists beyond 7 ns. This is in contrast to the instrument limited ESA observed at 460 nm for ZrO_2-**P1** following direct excitation of **P1** at 512 nm (blue in Figure 4c). We attribute the slow growth of ^{3}**PX*** features in the ZrO_2-**A**-Zn-**PX** films to a mechanism consisting of excitation of **A**, ^{1}**A*** to **PX** FRET, rapid intersystem crossing from ^{1}**PX*** to ^{3}**PX***, followed by slow excited state decay from ^{3}**PX***. It is important to note that our previous surface dilution studies indicate that the rapid energy transfer in the ZrO_2-**A**-Zn-**P3** film is dominated by inter-assembly energy transfer (i.e., between metal ion linked molecules) and not inter-layer energy transfer (i.e., between separate layers of non-linked molecules).[41] Consequently, the energy transfer dynamics measured here are likely dictated by the relative structure of the molecules within the metal ion linked assemblies.

The weighted average lifetime and rate constant for the appearance of ^{3}**PX*** (i.e., k_{FRET}) in ZrO_2-**A**-Zn-**PX** were obtained from a biexponential fit and the data are summarized in Table S2. The k_{FRET} increases in the order **P3** (0.6×10^{10} s^{-1}) < **P2** (2.4×10^{10} s^{-1}) ≈ **P1** (2.4×10^{10} s^{-1}). The trend again reveals an expected decrease in k_{FRET} with increasing distance (r_{DA} in equation 1) between the donor (**A**) and acceptor (**PX**). While the trend is generally reproducible across several sets of samples, it is important to acknowledge that the lifetime for **P1** and **P2** are similar within measurement standard deviation. Furthermore, the difference in k_{FRET} between ZrO_2-**A**-Zn-**P1** and ZrO_2-**A**-Zn-**P2** is smaller than one might expect for an r_{DA}^6 distance dependence. This observation suggests that distance is not the only FRET relevant parameter changing between the two samples, and that the relative orientation of the chromophores

View Article Online
DOI: 10.1039/D4TA05156D

in the assembly may also change due the presence of an additional phenylene spacer.

As an aside, we also investigated the ^{3}**PX*** to **A** triplet energy transfer (TET) using time-resolved emission from ^{3}**PX*** and the results are summarized in Figure S7 and Table S3. Consistent with the results above, the TET energy transfer rate for ZrO_2-**A**-Zn-**PX** increases in the order of **P3** (4.5×10^3 s^{-1}) < **P2** (7.0×10^3 s^{-1}) < **P1** (9.8×10^3 s^{-1}). This also agrees with the expectation of slowed TET with increasing r_{DA}.[54] Worth noting is that the necessity of orbital overlap for electron transfer suggests TET could also exhibit an orientation dependence[55–57] but experimental support for such phenomenon is limited.

Planar vs. Mesoporous Substrates

Spectroscopic measurements, like those in the previous section, as well as light harvesting/generating applications of molecule-metal oxide interfaces typically rely on mesoporous, fused nanoparticle substrates. This choice is due to their high surface areas, enabling increased absorption cross-section and amplified signals.[29] In contrast, a majority of techniques used to determine the structure of molecule-metal oxide interfaces, including those discussed below, are performed on planar substrates.[20,58,59] The underlying, but untested assumption is that the structure at the molecule-metal oxide interface is the same on planar (p-) and mesoporous (m-) substrates. Here we use **A** to **P3** FRET in the **A**-Zn-**P3** bilayer as an indirect probe of the interfacial structure on planar and mesoporous ZrO_2. Due to the inherent technical challenges of performing TA on planar substrates (i.e., low absorption and ΔA), we relied on time-resolved emission of the ZrO_2-**A**-Zn-**P3** bilayer, where k_{FRET} was sufficiently slowed and resolvable by our TCSPC emission measurement.

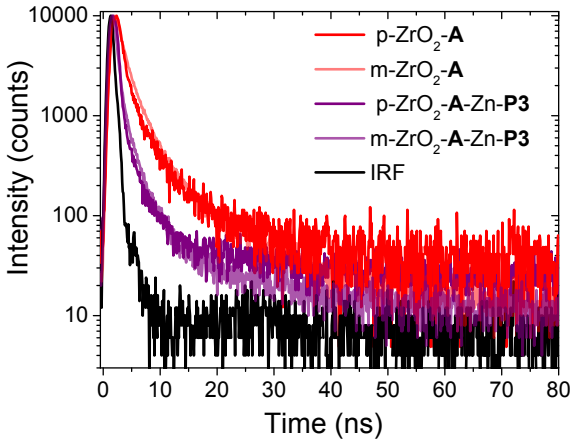

Fig. 5 Time-resolved emission decays at 460 nm for planar (p-) and mesoporous (m-) ZrO_2-**A** and ZrO_2-**A**-Zn-**P3** in MeCN (λ_{ex}=360 nm).

Following 360 nm excitation, ^{1}**A*** emission decay kinetics for **A** and **A**-Zn-**P3** films on p-ZrO_2 and m-ZrO_2 were measured, and the results are show in Figure 5 with kinetic fitting parameters summarized in Table S4. Both substrates exhibit similar kinetics for both the monolayer and bilayer films. From the fits to the data, the average lifetimes, and equation 4, similar k_{FRET} of $1.3\pm0.1 \times 10^8$ s^{-1} and $1.0\pm0.4 \times 10^8$ s^{-1} were determined for bilayers on p-ZrO_2 and m-ZrO_2, respectively. Given that each film has the same solvent (n) and chromophore pair (i.e., constant J and Φ_D), this observation suggests that r_{DA} and κ^2 are similar for the **A** and **P3** pair, regardless of the nature of the underlying substrate. This data strongly suggests that the structure of the bilayer film is similar on both planar and mesoporous substrates and that structural measurements on a planar surface (*vide infra*) can serve as a reasonable surrogate for mesoporous films.

Polarized Attenuated Total Reflectance

Insights into the structure of the ZrO_2-**A**-Zn-**PX** bilayers were obtained using polarized UV-Vis attenuated total reflectance spectroscopy (p-ATR).[31,60–62] p-ATR is performed by binding the molecule to a metal oxide coated glass waveguide that enables multiple internal reflections at the metal oxide-molecule-solvent interface. Then, the difference in attenuated absorption between transverse electric and transverse magnetic UV-Vis light can be used to determine the mean tilt angles of the transition dipole moment (θ_{tilt}) of chromophores relative to the surface normal. ITO, as opposed to ZrO_2 (*vide supra*), was used as the metal oxide substrate because highly planar films on waveguiding glass slides (i.e., RMS surface roughness of 0.5 ± 0.1 nm) are commercially available.[23,25] Importantly, our recent study shows that at high surface coverage, the orientation of molecules is similar regardless of the nature of the metal oxide (e.g., ITO, TiO_2, ZrO_2) indicating that ITO can serve as a reasonable surrogate for ZrO_2.[23]

p-ATR was used to monitor the multilayer assembly process and measure the surface coverage and θ_{tilt} of the chromophore films. Results are summarized in Table 2 with additional data and experimental data/details provided in the supporting information. Consistent with previous reports,[23–25] the **A** films achieve a hexagonal closest packed surface loading of ~3×10^{-10} mol/cm^2 and a tilt angle of ~30°, which slightly increase with Zn (~35°), and **PX** (~37°) coordination. **P1-3** loaded on the ITO-**A**-Zn with a surface coverage of ~3×10^{-11} mol/cm^2, resulting in an ~10:1, **A**:**PX** loading ratio as observed on m-ZrO_2. Interestingly, the tilt angle of the porphyrin (i.e., the plane of the porphyrin core) relative to surface normal increases in the order of **P3** (22°) < **P2** (36°) < **P1** (50°) in the ITO-**A**-Zn-**PX** films.

Table 2. Surface coverages and mean tilt angle (θ_{tilt}) of **A**, **A**-Zn, and **A**-Zn-**PX** adsorbed on ITO as determined from p-ATR.[a]

Film on ITO	θ_{tilt} (°)	Surface coverage (mol/cm²)
A	30 ± 1[b]	$3.1\pm0.2 \times 10^{-10}$ [b]
A in (**A**-Zn)	35 ± 3[b]	
A in (**A**-Zn-**P1**)	37 ± 3[b]	
P1 in (**A**-Zn-**P1**)	50 ± 1	$2.8\pm0.9 \times 10^{-11}$
P2 in (**A**-Zn-**P2**)	36 ± 2	$5\pm2 \times 10^{-11}$
P3 in (**A**-Zn-**P3**)	22 ± 4	$3\pm2 \times 10^{-11}$

View Article Online
DOI: 10.1039/D4TA05156D

[a] For all cases, n=3 trials and the error is the standard deviation of the three trials. [b] Results from the **A**-Zn-**P1** bilayer. **A** surface coverage and θ_{tilt} data from the **A**-Zn-**P2** and **A**-Zn-**P3** bilayers are provided in the supporting information.

Based on the p-ATR data, a depiction of the molecular orientations relative to the ITO surface normal for ITO-**A**-Zn-**PX** films are shown in Figure 6. To generate these drawings, the tilt angle for **A** is depicted using the transition dipole across the 9,10-carbon atoms of the anthracene[43,63] and for **PX**, the plane of the porphyrin core is used and assumed it is aligned with the axis of the phenyl carboxylate linker.[49,64]

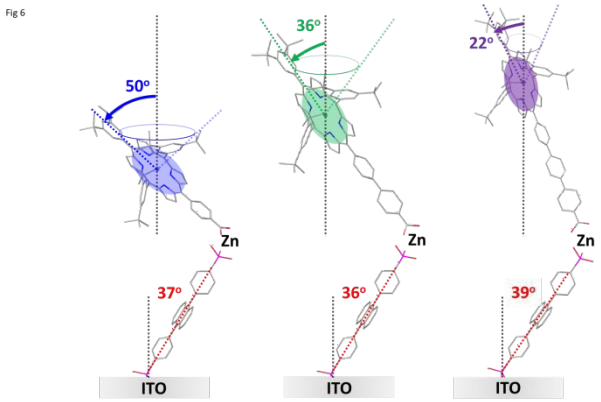

Fig. 6 Schematic representation of the mean polar tilt angles for **A** and **PX** in **A**-Zn-**P1** (left), **A**-Zn-**P2** (middle), and **A**-Zn-**P3** (right) on ITO. Cones represent possible porphyrin orientations assuming the plane of the porphyrin is aligned with the axis of the phenyl carboxylate linker.

While some structural insights were obtained from this measurement, two critical points must be made. First, even in the absence of an exact structure, the porphyrin plane angle changes between the three bilayers. Consequently, κ^2 is not constant, so the number of phenylene spacers (i.e., r_{DA}) and FRET efficiency cannot be used to determine the relative orientation between the chromophores uniformly across the series. Second, for a chromophore with a single transition dipole moment, a cone is sufficient to capture all possible angles of the second layer chromophore relative to the surface normal and first chromophore. However, as we will discuss in the next section, the transition plane of the porphyrin greatly expands the range of possible structures.

FRET Efficiency and Structure

As noted above, p-ATR only provides information about the orientation of the porphyrin plane relative to the surface normal. Therefore, even the cone angle depicted in Figure 6 is insufficient to capture all possible orientations of the porphyrin plane. To explore possible structures, we performed geometric calculations with key structural parameters shown in Figure 7 (see SI for details). The model consists of vector representations for **A** and **PX** in red and purple, respectively (Figure 7a), arranged in all possible relative orientations (Figure 7b), onto which vector representations of the transition dipoles were then superimposed (Figure S15). This analysis was performed in three steps: 1) establishing a full set of possible geometries where the transition dipole vectors of **A** and **PX** agree with the angles determined by p-ATR, 2) calculating the FRET efficiency for each of the geometries using equations 1-3, and 3) comparing calculated and experimental efficiencies to determine the most probable orientation.

To begin, we assume that **A** is oriented at a fixed angle (θ_A) relative to the surface normal, as determined by p-ATR, and that the Zn-ion acts as a stationary vertex around which **PX** can freely rotate. In our model, the Zn linker ion is set as the origin of coordinates, surface normal is set as the z-axis, and the vector representation of **A** (r_A) is set in the x,z-plane. The free motion of the vector model for **PX** (r_P) consists of azimuthal (ϕ) and altitudinal (θ_P) rotations, giving a theoretical sphere which r_P can trace (Figure 7b). Additionally, free rotation of the porphyrin plane about the meso-axis (θ_{rot}) allows **PX** to adopt geometries outside of the cone depicted in Figure 6. Given the constraint that the maximum gradient of the porphyrin plane must be at the angle θ_{tilt} from surface normal, the set of possible orientations for **PX** is restricted to a spherical frustum shown in Figure S15.

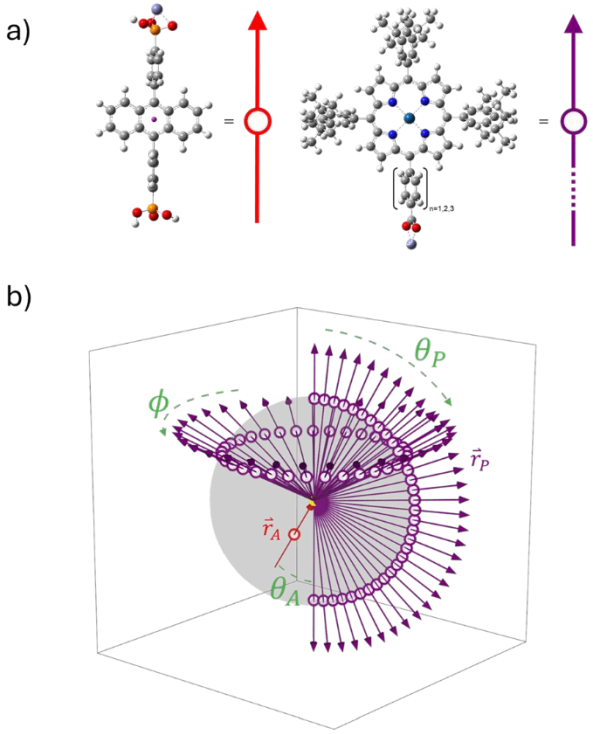

Fig. 7 a) Vector representations of the transition dipole moments of **A** (red) and **PX** (purple) with the chromophore centroid depicted as a circle. (b) Geometric orientation of vectors showing permutation by altitudinal (θ_P) and azimuthal (ϕ) rotation. In this model space, θ_P is defined as the angle to the positive z-axis and ϕ is defined as the angle between the projection of r_P onto the x,y-plane and the positive x-axis

Using equations 1 and 2 with κ^2 and r_{DA} from the model structures, as well as $J = 2 \times 10^{-14}$, $\Phi_D = 0.53$, and n =1.36 from

View Article Online
DOI: 10.1039/D4TA05156D

experimental values[40,65] we calculated theoretical FRET efficiencies (E_{theo}) for all of the geometries and the results are shown in Figure 8a and Figure S16a-b. In line with prior literature,[66] for these calculations we used the average κ^2 from two perpendicular, degenerate transition dipole moments of the porphyrin plane (i.e., one aligned with the long axis and one perpendicular through the meso-carbons).

The surfaces of E_{theo} for the **A**-Zn-**PX** models generally look similar (Figure S16a-c) but with differences in amplitude of E_{theo}. Particularly notable is that in the case of **P1**, the short r_{DA} leads to high E_{theo} (>0.99) across a majority of the surface (Figure S16a). In contrast, a larger variation in E_{theo} is observed for the bilayer containing **P2** (Figure S16b) and **P3** (Figure 8a).

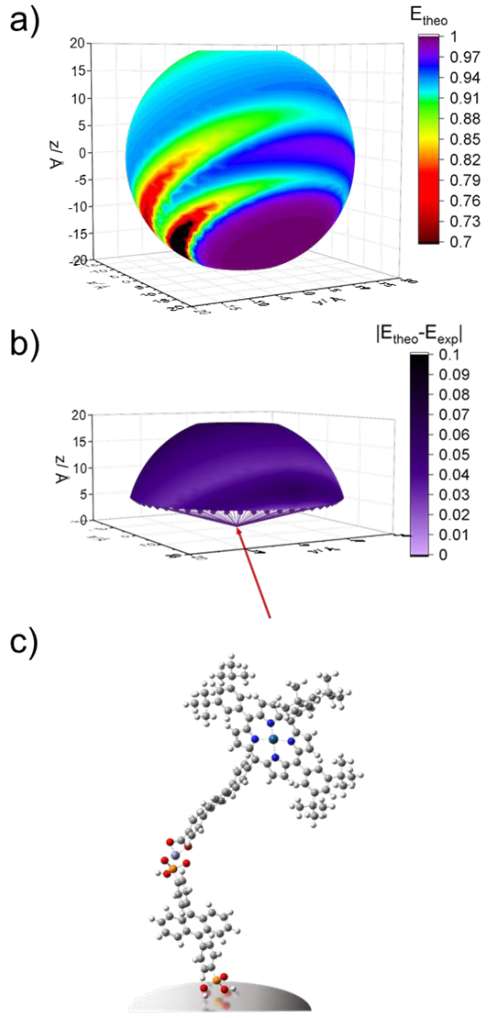

Fig. 8 a) Calculated **A** to **P3** FRET efficiencies for ZrO_2-**A**-Zn-**P3** where θ_A is 39° and **P3** is oriented at all geometries with a porphyrin core plane angle of 22° relative to surface normal. b) Heatmap depicting absolute difference between theoretical and experimental FRET efficiencies. c) Example geometry of a bilayer orientation within the feasible band (θ_P = 53°,ϕ = 21°,θ_{rot} = 62°).

To determine the geometries that are most consistent with the experimentally determined FRET efficiencies (E_{exp}), we constructed heatmaps showing the absolute difference between E_{theo} and E_{exp} (Figure S16g-i). For these heatmaps, E_{exp} was calculated using equation 4

$$E_{exp} = \frac{\frac{k_{FRET}}{k_r+k_{nr}}}{1-\frac{k_{FRET}}{k_r+k_{nr}}} \qquad (4)$$

where k_{FRET} is the FRET rate constant for each ZrO_2-**A**-Zn-**PX** film (*vide supra*), and k_r (8.8 x 10^7 s^{-1}) and k_{nr} (7.8 x 10^7 s^{-1}) are the intrinsic radiative and non-radiative rate constants, respectively, for **PX**. From this equation we obtain an energy transfer efficiency of 0.99, 0.99, and 0.97 for bilayers containing **P1**, **P2**, and **P3**, respectively. Note that because k_{FRET} was determined from the ultrafast TA measurements, it only captures dynamics/yields of intra-assembly energy transfer,[41] and in-turn structural aspects of the metal ion linked donor-acceptor pair.

The heatmaps for $|E_{theo}-E_{exp}|$ were then projected onto the spherical sections and the results are shown in Figure 8b and Figure S16g-i. The lower portions of the spheres were omitted (x < 5Å) because it is assumed that due to steric constraints, **PX** is unable to adopt geometries that would place the 3,5-di-tert-butylbenzene groups deep within the ZrO_2-**A**-Zn sublayers.

For the **A**-Zn-**P1** bilayer, there is a broad range of possible geometries that show agreement between calculated and experimental values ($|E_{theo}-E_{exp}|$<0.01). In contrast, for bilayers containing **P2** (Figure S16h) and **P3** (Figure 8b), there is an apparent radial band across the sphere indicating that those structures exhibit stronger agreement between E_{theo} and E_{exp}. Among the possible geometries we selected example structures that show the best theoretical-experimental agreement, and those structures are depicted in Figure 8c for ZrO_2-**A**-Zn-**P3** with the remaining structures in Figure S16.

Conclusions

Here we prepare metal ion-linked bilayer films containing a series of platinum porphyrin derivatives with one (**P1**), two (**P2**), or three (**P3**) phenylene spacers between the chromophoric core and the metal ion binding carboxylate group. The porphyrins were bound to a phosphonated anthracene (**A**) functionalized mesoporous ZrO_2 surface with a Zn(II) linking ion to generate the ZrO_2-**A**-Zn-**PX** bilayer films. Both time-resolved emission and transient absorption measurements indicate that the rate and efficiency of **A*** to **PX** FRET generally decrease in the order of **P1** ≥ **P2** >**P3**. With the FRET efficiency in hand, our goal was to use known parameters in the FRET equation (i.e., overlap integral, refractive index, and fluorescence quantum yield of the donor), combined with a systematic change in r_{DA} with phenylene spacer length, to calculate the orientation factor (κ^2) across the series. This method assumes that κ^2 is the same for all three bilayers. However, UV-Vis polarized visible attenuated total reflectance (p-ATR) indicate that the tilt angle of the porphyrin relative to surface normal increases in the

View Article Online
DOI: 10.1039/D4TA05156D

order of **P3** (22°) < **P2** (36°) < **P1** (50°). Consequently, the interchromophore distance and orientation are changing with each bilayer and thus the method described above cannot be used to determine κ^2 across the series.

Furthermore, p-ATR only provides information regarding the orientation of the porphyrin plane relative to the surface normal which greatly expands the possible orientations of the long axis of the molecule relative to **A**. To narrow the scope of possible structures, we performed geometric calculations of all possible structures that agree with the angles determined p-ATR and determined the theoretical FRET efficiency of each geometry. Then by comparing calculated and experimental efficiencies we proposed the most likely structures of the bilayer films.

Additionally, we compared the energy transfer rate of **A**-Zn-**P3** bilayers on mesoporous and planar ZrO_2 substrates. The nearly identical energy transfer rate indicates that the structure of the bilayer is similar, regardless of the nature of the underlying substrate. This observation is critical in that, despite decades of assuming the structures are the same, this report provides strong evidence that the structure is consistent on planar and mesoporous substrates, and each can serve as a reasonable surrogate for the other.

In summary, while we were unable to determine an absolute structure, this work provides new structural insights into multilayer films on planar and mesoporous surfaces. Additionally, we demonstrate the promise of p-ATR and FRET as complementary techniques to determine the structure of multichromophore assemblies. Going forward, the use of an acceptor chromophore with a single transition dipole moment (i.e., not a porphyrin) will dramatically narrow the possible range of structures and will enable the determination of a single, likely structure of the bilayer assembly. Furthermore, with these tools in hand, we look forward to investigating the role of variables like metal ion binding motif, surface coverage, linking metal ion, etc. in dictating the structure of these multilayer assemblies. With increased insights, one can envision controlling such structures to design assemblies that facilitate or hinder energy and electron transfer processes, for example, as desired for a given application.

Conflicts of interest

There are no conflicts to declare.

Data availability

The data supporting this article have been included as part of the Supplementary Information.

Acknowledgements

Energy transfer measurements were supported by the National Science Foundation under Grant No. DMR-2327754. Characterization of the bilayer formation was supported by the Army Research Office under Grant No. W911NF-19-1-0357. A.I. is grateful to the National Science Foundation (CHE-2102579) for the support of fundamental research. A.A. acknowledges the Arnold O. Beckman Postdoctoral Fellowship Program. Some of the ATR data were acquired in the W.M. Keck Center for Nano-Scale Imaging in the Department of Chemistry and Biochemistry at the University of Arizona. This instrument was supported as part of the Center for Interface Science: Solar-Electric Materials (CIS:SEM), an Energy Frontier Research Center funded by the U.S. Department of Energy, Office of Science, Office of Basic Energy Sciences under Award No. DE-SC0001084.

References

1 S. P. Pujari, L. Scheres, A. T. M. Marcelis and H. Zuilhof, *Angew. Chem. Int. Ed.*, 2014, **53**, 6322–6356.
2 E. Galoppini, *Coord. Chem. Rev.*, 2004, **248**, 1283–1297.
3 A. Arcidiacono, B. Hanks and K. Hanson, *ACS Appl. Opt. Mater.*, 2023, **1**, 1156–1168.
4 J. C. Wang, S. P. Hill, T. Dilbeck, O. O. Ogunsolu, T. Banerjee and K. Hanson, *Chem. Soc. Rev.*, 2018, **47**, 104–148.
5 Y. Zhou, C. Ruchlin, A. J. Robb and K. Hanson, *ACS Energy Lett.*, 2019, **4**, 1458–1463.
6 S. P. Hill, T. Dilbeck, E. Baduell and K. Hanson, *ACS Energy Lett.*, 2016, **1**, 3–8.
7 D. Beery, T. W. Schmidt and K. Hanson, *ACS Appl. Mater. Interfaces*, 2021, **13**, 32601–32605.
8 O. O. Ogunsolu, I. A. Murphy, J. C. Wang, A. Das and K. Hanson, *ACS Appl. Mater. Interfaces*, 2016, **8**, 28633–28640.
9 X. Ding, Y. Gao, L. Zhang, Z. Yu, J. Liu and L. Sun, *ACS Catal.*, 2014, **4**, 2347–2350.
10 N. Yoshimura, M. Yoshida, M. Kato and A. Kobayashi, *Inorg. Chem.*, 2022, **61**, 11095–11102.
11 M. A. Gross, C. E. Creissen, K. L. Orchard and E. Reisner, *Chem. Sci.*, 2016, **7**, 5537–5546.
12 O. O. Ogunsolu, J. C. Wang and K. Hanson, *ACS Appl. Mater. Interfaces*, 2015, **7**, 27730–27734.
13 J. C. Wang, I. A. Murphy and K. Hanson, *J. Phys. Chem. C*, 2015, **119**, 3502–3508.
14 B. H. Farnum, K.-R. Wee and T. J. Meyer, *Nat. Chem.*, 2016, **8**, 845–852.
15 R. N. Sampaio, L. Troian-Gautier and G. J. Meyer, *Angew. Chem.*, 2018, **130**, 15616–15620.
16 Z.-J. Li, C.-J. Yao and Y.-W. Zhong, *Sci. China Chem.*, 2019, **62**, 1675–1685.
17 A. Arcidiacono, A. J. Robb, R. A. Masitas, S. R. Salpage, G. M. McLeod, J. Chen, O. O. Ogunsolu, M. G. Roper and K. Hanson, *J. Photochem. Photobiol.*, 2022, **9**, 100088.

18 K. Hanson, D. A. Torelli, A. K. Vannucci, M. K. Brennaman, H. Luo, L. Alibabaei, W. Song, D. L. Ashford, M. R. Norris, C. R. K. Glasson, J. J. Concepcion and T. J. Meyer, *Angew. Chem. Int. Ed.*, 2012, **51**, 12782–12785.

19 A. J. Robb, D. Miles, S. R. Salpage, N. Watson, Q. He, Q. Wu and K. Hanson, *ACS Appl. Mater. Interfaces*, 2020, **12**, 38003–38011.

20 B. Tosco, B. P.-A. V. Melo, D. Hermida Merino, J. F. Q. Rey and S. Brochsztain, *Langmuir*, 2021, **37**, 2494–2502.

21 H. C. Yang, K. Aoki, H. G. Hong, D. D. Sackett, M. F. Arendt, S. L. Yau, C. M. Bell and T. E. Mallouk, *J. Am. Chem. Soc.*, 1993, **115**, 11855–11862.

22 H. Byrd, J. L. Snover and M. E. Thompson, *Langmuir*, 1995, **11**, 4449–4453.

23 D. Pattadar, L. Zheng, A. J. Robb, D. Beery, W. Yang, K. Hanson and S. S. Saavedra, *J. Phys. Chem. C*, 2023, **127**, 2705–2715.

24 A. Arcidiacono, Y. Zhou, W. Zhang, J. O. Ellison, S. Ayad, E. S. Knorr, A. N. Peters, L. Zheng, W. Yang, S. S. Saavedra and K. Hanson, *J. Phys. Chem. C*, 2020, **124**, 23597–23610.

25 D. Pattadar, A. Arcidiacono, D. Beery, K. Hanson and S. S. Saavedra, *Langmuir*, 2023, **39**, 10670–10679.

26 M. J. Griffith, M. James, G. Triani, P. Wagner, G. G. Wallace and D. L. Officer, *Langmuir*, 2011, **27**, 12944–12950.

27 M. Gliboff, L. Sang, K. M. Knesting, M. C. Schalnat, A. Mudalige, E. L. Ratcliff, H. Li, A. K. Sigdel, A. J. Giordano, J. J. Berry, D. Nordlund, G. T. Seidler, J.-L. Brédas, S. R. Marder, J. E. Pemberton and D. S. Ginger, *Langmuir*, 2013, **29**, 2166–2174.

28 L. Sang, A. Mudalige, A. K. Sigdel, A. J. Giordano, S. R. Marder, J. J. Berry and J. E. Pemberton, *Langmuir*, 2015, **31**, 5603–5613.

29 A. J. Robb, E. S. Knorr, N. Watson and K. Hanson, *J. Photochem. Photobiol. Chem.*, 2020, **390**, 112291.

30 W. J. Doherty, C. L. Donley, N. R. Armstrong and S. S. Saavedra, *Appl. Spectrosc.*, 2002, **56**, 920–927.

31 S. B. Mendes, J. T. Bradshaw and S. S. Saavedra, *Appl. Opt.*, 2004, **43**, 70–78.

32 T. Dilbeck, J. C. Wang, Y. Zhou, A. Olsson, M. Sykora and K. Hanson, *J. Phys. Chem. C*, 2017, **121**, 19690–19698.

33 Y. Zhou, S. Ayad, C. Ruchlin, V. Posey, S. P. Hill, Q. Wu and K. Hanson, *Phys. Chem. Chem. Phys.*, 2018, **20**, 20513–20524.

34 L. Stryer and R. P. Haugland, *Proc. Natl. Acad. Sci. U. S. A.*, 1967, **58**, 719–726.

35 Th. Förster, *Ann. Phys.*, 1948, **437**, 55–75.

36 J. R. Lakowicz, *Principles of Fluorescence Spectroscopy*, Springer Science & Business Media, 2013.

37 V. Gray, B. Küçüköz, F. Edhborg, M. Abrahamsson, K. Moth-Poulsen and B. Albinsson, *Phys. Chem. Chem. Phys.*, 2018, **20**, 7549–7558.

38 V. Gray, K. Börjesson, D. Dzebo, M. Abrahamsson, B. Albinsson and K. Moth-Poulsen, *J. Phys. Chem. C*, 2016, **120**, 19018–19026.

39 S.-H. A. Lee, N. M. Abrams, P. G. Hoertz, G. D. Barber, L. I. Halaoui and T. E. Mallouk, *J. Phys. Chem. B*, 2008, **112**, 14415–14421.

40 S. P. Hill, T. Banerjee, T. Dilbeck and K. Hanson, *J. Phys. Chem. Lett.*, 2015, **6**, 4510–4517.

41 G. M. McLeod, J. Nolder, A. Arcidiacono, S. Lindbom, N. Dos Santos, E. Lambert, S. Ayad, D. Beery, I. Alabugin and K. Hanson, *J. Phys. Chem. C.*, 2024, ASAP, 10.1021/acs.jpcc.4c04033

42 Y. Zheng, A. J. Giordano, R. C. Shallcross, S. R. Fleming, S. Barlow, N. R. Armstrong, S. R. Marder and S. S. Saavedra, *J. Phys. Chem. C*, 2016, **120**, 20040–20048.

43 B. Norden, G. Lindblom and I. Jonas, *J. Phys. Chem.*, 1977, **81**, 2086–2093.

44 S. P. Hill and K. Hanson, *J. Am. Chem. Soc.*, 2017, **139**, 10988–10991.

45 P. Bharmoria, H. Bildirir and K. Moth-Poulsen, *Chem. Soc. Rev.*, 2020, **49**, 6529–6554.

46 Y. Zhou, S. P. Hill and K. Hanson, *J. Photonics Energy*, 2017, **8**, 022004.

47 J. S. Lindsey, *Acc. Chem. Res.*, 2010, **43**, 300–311.

48 P. Mishra, J. P. Hill, S. Vijayaraghavan, W. V. Rossom, S. Yoshizawa, M. Grisolia, J. Echeverria, T. Ono, K. Ariga, T. Nakayama, C. Joachim and T. Uchihashi, *Nano Lett.*, 2015, **15**, 4793–4798.

49 M. Gouterman, *J. Mol. Spectrosc.*, 1961, **6**, 138–163.

50 R. Katoh, A. Furube, T. Yoshihara, K. Hara, G. Fujihashi, S. Takano, S. Murata, H. Arakawa and M. Tachiya, *J. Phys. Chem. B*, 2004, **108**, 4818–4822.

51 J. R. Durrant, S. A. Haque and E. Palomares, *Coord. Chem. Rev.*, 2004, **248**, 1247–1257.

52 Y. Venkatesh, M. Venkatesan, B. Ramakrishna and P. R. Bangal, *J. Phys. Chem. B*, 2016, **120**, 9410–9421.

53 S. M. Aly, S. Goswami, Q. A. Alsulami, K. S. Schanze and O. F. Mohammed, *J. Phys. Chem. Lett.*, 2014, **5**, 3386–3390.

54 D. L. Dexter, *J. Chem. Phys.*, 1953, **21**, 836–850.

55 H. S. Judeikis and S. Siegel, *J. Chem. Phys.*, 1970, **53**, 3500–3506.

56 J. K. Roy and M. A. El-Sayed, *J. Chem. Phys.*, 1964, **40**, 3442–3443.

View Article Online
DOI: 10.1039/D4TA05156D

57 K. B. Eisenthal, *J. Chem. Phys.*, 1969, **50**, 3120–3122.
58 V. Kaliginedi, H. Ozawa, A. Kuzume, S. Maharajan, I. V. Pobelov, N. Hee Kwon, M. Mohos, P. Broekmann, K. M. Fromm, M. Haga and T. Wandlowski, *Nanoscale*, 2015, **7**, 17685–17692.
59 H. E. Katz, W. L. Wilson and G. Scheller, *J. Am. Chem. Soc.*, 1994, **116**, 6636–6640.
60 L. E. Oquendo, R. Ehamparam, N. R. Armstrong, S. S. Saavedra and D. V. McGrath, *J. Phys. Chem. C*, 2019, **123**, 6970–6980.
61 R. Ehamparam, L. E. Oquendo, M. W. Liao, A. K. Brynnel, K.-L. Ou, N. R. Armstrong, D. V. McGrath and S. S. Saavedra, *ACS Appl. Mater. Interfaces*, 2017, **9**, 29213–29223.
62 P. L. Edmiston, J. E. Lee, S.-S. Cheng and S. S. Saavedra, *J. Am. Chem. Soc.*, 1997, **119**, 560–570.
63 H. Inoue, T. Hoshi, T. Masamoto, J. Shiraishi and Y. Tanizaki, *Berichte Bunsenges. Für Phys. Chem.*, 1971, **75**, 441–446.
64 J. A. Shelnutt and V. Ortiz, *J. Phys. Chem.*, 1985, **89**, 4733–4739.
65 S. S. Saavedra and W. M. Reichert, *Anal. Chem.*, 1990, **62**, 2251–2256.
66 J. Mårtensson, *Chem. Phys. Lett.*, 1994, **229**, 449–456.

View Article Online
DOI: 10.1039/D4TA05156D

The data supporting this article have been included as part of the Supplementary Information.